Research Square

Preprints are preliminary reports that have not undergone peer review.
They should not be considered conclusive, used to inform clinical practice,
or referenced by the media as validated information.

On the absence of the generating function and its implications for the convergence region of the interior spherical Bessel gravity field

Yu Takahashi

yu.takahashi@jpl.nasa.gov

Jet Propulsion Laboratory

Research Article

Keywords:

Posted Date: November 11th, 2026

DOI: https://doi.org/10.21203/rs.3.rs-11416725/v1

License: This work is licensed under a Creative Commons Attribution 4.0 International License.
Read Full License

Additional Declarations: No competing interests reported.

On the absence of the generating function and its implications for the convergence region of the interior spherical Bessel gravity field

Yu Takahashi[1*]

[1*]Mission Design and Navigation, Jet Propulsion Laboratory, California Institute of Technology, 4800 Oak Grove Dr., Pasadena, 91109, California, U.S.A.

Corresponding author(s). E-mail(s): yu.takahashi@jpl.nasa.gov;

Abstract

It is a well known fact that the conventional exterior gravity field only converges outside the Brillouin (circumscribing) sphere. The counterpart of this gravity model is the interior spherical Bessel gravity field that converges within the Brillouin sphere. These two gravity fields allow for global modeling of the gravity by alternating at the Brillouin sphere. The divergence of the exterior gravity field within the Brillouin sphere is understood by expanding the potential definition with the generating function for the Legendre polynomial. We note that there is no equivalent expression with the generating function that leads us to the interior spherical Bessel harmonics. We believe that the lack of the generating function for the interior spherical Bessel gravity field, which confers the convergence region of the gravity model, can be leveraged to our advantage. We show that the convergence region of the interior spherical Bessel harmonics can be arbitrarily made larger than the physical Brillouin radius, thereby increasing the convergence region beyond the Brillouin sphere. This allows us to avoid alternating between the two gravity models and simply use the interior spherical Bessel gravity field at all times for global gravity modeling.

Keywords: Gravity, Spherical Harmonics, Small Bodies, Reference Radius, Convergence Region, Brillouin Sphere

1 Introduction

Thorough descriptions of various gravity models are summarized in Takahashi et al. [1], and the readers are referred to their manuscript for the origins/applications of different gravity models. This manuscript is the continuation of their work that illuminates the remarkable properties of the interior spherical Bessel gravity field. For this introduction, it suffices that we summarize two fundamental equations: Laplace's and Poisson's equations.

Fundamentally, the gravitational model (i.e., the mathematical framework) of a celestial body must satisfy Laplace's equation, Poisson's equation, or both depending on the location of the evaluation point. Laplace's equation is presented below:

$$\nabla^2 U = 0, \tag{1}$$

where U is the gravitational potential. This condition needs to be satisfied at all points outside the celestial body. Because Eq. 1 is a second-order differential equation, it yields two solutions. A universal model of this type is the *exterior* spherical harmonic gravity field (to be discussed in detail in the next section), and the other is the *interior* spherical harmonic gravity field (e.g., [2] and [3]).

Inside the body, Poisson's equation dictates the gravitational potential:

$$\nabla^2 U = -4\pi G\rho, \tag{2}$$

where G is the gravitational constant and ρ is the density of the body at the evaluation point. Of course, the density is zero outside the body and Poisson's equation reduces to Laplace's equation. Similarly to the Laplace's equation, Poisson's equation also yields two solutions: *interior* and *exterior* spherical Bessel gravity fields [4]. Both of the two spherical Bessel gravity fields are spherical harmonic gravity fields. Thus, by solving for Eqs. 1 and 2 in spherical coordinates, we obtain four sets of spherical harmonic gravity fields. All of the four spherical harmonic gravity fields only satisfy either Laplace's or Poisson's equations from which they are derived.

Perhaps because the interior spherical Bessel gravity field is relatively unknown and the exterior gravity field is historically used for *all* spacecraft missions, the common mistake is to still use the exterior gravity field within the Brillouin sphere (i.e., circumscribing sphere [5]) when necessary. Although there are mitigation techniques (e.g., truncating the degree/order of the infinite series) and the degree of divergence can be characterized (e.g., Kholshevnikov [6], Šprlák and Han [7], Hirt and Kuhn [8], and Bevis et al. [9]), the computed potential/acceleration are still erroneous by definition.

One remark often made in this context is that the Laplacian of the exterior gravity field yields zero in space between the surface and the Brillouin sphere, representing the physical reality. However, we note that the implicit assumption made when solving for Laplace's equation (Eq. 1) is that there is mass in other regions, which is *everywhere* inside the Brillouin sphere (i.e., Poisson's equation). That is, the mass exists or does not exists at the evaluatoin point due to the nature of solving for Laplace's and

Poisson's equations in the spherical coordinates. As such, satisfying the Laplace's equation inside the Brillouin sphere via the exterior spherical harmonic gravity field is contradictory to its assumption.

If the spherical harmonic expansion is not desired, then there are other alternatives, such as the polyhedral gravity field [10]. This gravity field satisfies both Laplace's and Poisson's equations depending on the evaluation point and it can model the gravity field globally if the density distribution within the body is known. However, it is common knowledge that the density distribution within a body is difficult to obtain.

In the next few sections we further investigate the origin of the series divergence for the exterior gravity field in order to unravel the convergence properties of the interior spherical Bessel gravity field. We claim that the previously held idea that the interior spherical Bessel gravity field only converges within the Brillouin sphere is false. Instead, we can make the convergence region arbitrarily larger (but not smaller) than the Brillouin sphere by scaling the boundary sphere with the exterior gravity field. We will numerically prove this claim in the subsequent sections and lay the foundation for its application to orbit determination (OD) as a future work.

2 Derivation of the Exterior Gravity Field

The derivation of the exterior gravity field is well documented elsewhere [2, 11–15]. One method is the separation of variables to solve for the Laplace's equation. Although this method is straightforward, it lacks in rigor in a sense that the convergence region is not clearly informed during the derivation. Another method is to start from the potential definition and leverage the generating function of the Legendre polynomial. In this section we show where this generating function arises, borrowing from the derivation detailed in Werner [2] and Takahashi et al. [3].

The potential of a field point (i.e., spacecraft) under the influence of a body's gravity field is defined as

$$U = G\int_V \frac{\rho(\boldsymbol{r'})dV}{|\boldsymbol{r}-\boldsymbol{r'}|} = G\int_M \frac{1}{\Delta}dm', \tag{3}$$

where ρ is the density as a function of the position vector of a mass element ($\boldsymbol{r'}$), V is the total volume of the body, $\boldsymbol{r}$ is the field point position vector, M is the total mass of the body, and m' is the differential mass element at $\boldsymbol{r'}$, and $\boldsymbol{\Delta}$ is the relative position between the field point and the mass element (Fig. 1). We denote the quantities related to the differential mass element with a prime.

In Fig. 1, θ is the angle between $\boldsymbol{r}$ and $\boldsymbol{r'}$. By invoking the law of cosine, Eq. 3 is expressed as

$$U(r,\phi,\lambda) = G\int_M \frac{1}{\Delta}dm' = G\int_M \frac{1}{\sqrt{r^2+r'^2-2rr'\cos\theta}}dm'. \tag{4}$$

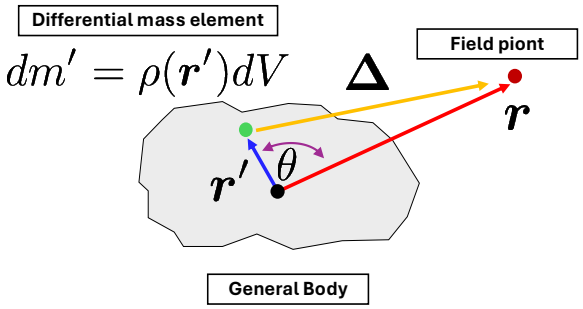


Fig. 1: Geometry for the potential definition.

Note that at this point we have not made distiction as to which of Laplace's or Poisson's equations we are solving for. Thus, Eq. 4 is a general expression. To solve for the exterior gravity field, we factor out r in Eq. 4:

$$U^e(r,\phi,\lambda) = G\int_M \frac{1}{r}\frac{1}{\sqrt{1-2\left(\frac{r'}{r}\right)\cos\theta+\left(\frac{r'}{r}\right)^2}}dm', \tag{5}$$

where the superscript e denotes the exterior quantity. The reason to factor out r is related to the convergence of the Legendre polynomial, which is defined as

$$P_n(\mu) = \frac{1}{2^n n!}\frac{d^n}{d\mu^n}(\mu^2-1)^n. \tag{6}$$

Here, $P_n(\mu)$ is the Legendre polynomial of degree n. This Legendre polynomial is expressed by the following generating function:

$$\frac{1}{\sqrt{1-2h\mu+h^2}} = \sum_{n=0}^{\infty} h^n P_n(\mu), \tag{7}$$

which converges absolutely and uniformly when $|h|<1$. By comparing this expression with Eq. 5, it is immediately found that $\mu=\cos\theta$ and $h=r'/r$ for the exterior gravity field. Then, substitution of Eq. 7 into Eq. 5 yields

$$U^e(r,\phi,\lambda) = G\int_M \sum_{n=0}^{\infty}\frac{(r')^n}{r^{n+1}}P_n(\cos\theta)dm'. \tag{8}$$

The sphere dictated by $|h| < 1$ is called the Brillouin sphere. Thus, Eq. 8 converges when the field point is outside the Brillouin sphere, the reason U^e is called the exterior gravity field. Note that the convergence region of the exterior gravity field is dictated by the farthest mass element of the body away from the coordinate center, as shown in Fig. 2:

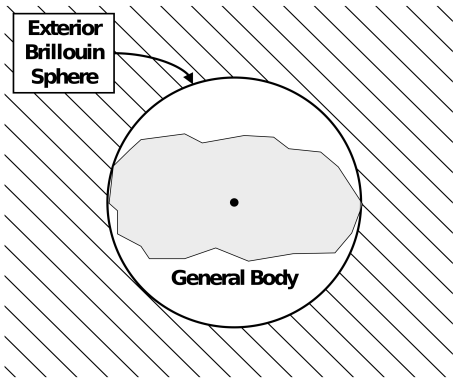


Fig. 2: Convergence region of the exterior gravity field.

By further invoking the addition theorem of the Legendre polynomial, we can write the exterior gravity field as follows:

$$U^e = \frac{GM^*}{R_e^*} \sum_{n=0}^{\infty} \sum_{m=0}^{n} \left(\frac{R_e^*}{r} \right)^{n+1} P_{nm}(\sin\phi) \begin{bmatrix} \cos(m\lambda) \\ \sin(m\lambda) \end{bmatrix} \cdot \begin{bmatrix} C_{nm}^e \\ S_{nm}^e \end{bmatrix}, \tag{9}$$

where U is the potential, e super/subscript denote the exterior quantity, G is the gravitational constant, M^* is the reference mass (nominally the total mass of the body), R^* is the reference radius (nominally the radius of the Brillouin sphere, explained below), r is the spacecraft position, P_{nm} is the associated Legendre function of degree n and order m, C_{nm}^e and S_{nm}^e are the exterior spherical harmonic coefficients, λ is longitude, and ϕ is latitude in the body-fixed frame. Note that, as detailed by Werner [2], the reference radius does not dictate the convergence and is arbitrary [1]. The divergence of the exterior gravity field within the Brillouin sphere arises from the generating function of the Legendre polynomial (Eq. 7), and is *baked into* the mass integral of coefficients C_{nm}^e and S_{nm}^e. These exterior spherical harmonics are defined as follows:

[1] Of course, when coding in a programming language, there is numerical precision we need to worry about. It is recommended to use the Brillouin radius as the reference radius.

$$\begin{cases} C^e_{nm} &= \dfrac{(2-\delta_{0,m})}{M^*}\dfrac{(n-m)!}{(n+m)!}\displaystyle\int_M \left(\frac{r'}{R^*_e}\right)^n P_{nm}(\sin\phi')\cos(m\lambda')dm', \\ S^e_{nm} &\overset{m\geq 0}{=} \quad \dfrac{2}{M^*}\dfrac{(n-m)!}{(n+m)!}\displaystyle\int_M \left(\frac{r'}{R^*_e}\right)^n P_{nm}(\sin\phi')\sin(m\lambda')dm'. \end{cases} \tag{10}$$

One convenient feature of the exterior spherical harmonics definition above is that the coefficients derived from two different reference radii ($R^*_{e,1}$ and $R^*_{e,2}$), both representing the same gravity field, are simply related by the following rule:

$$\begin{bmatrix} C^e_{nm,2} \\ S^e_{nm,2} \end{bmatrix} = \left(\frac{R^*_{e,1}}{R^*_{e,2}}\right)^n \begin{bmatrix} C^e_{nm,1} \\ S^e_{nm,1} \end{bmatrix}. \tag{11}$$

Since the reference radius cannot be deduced from the coefficients, that information must be supplied, for example, when comparing the coefficients between multiple gravity solutions. Because of Eq. 11, seemingly different estimates of the C^e_{nm}, S^e_{nm} harmonics could be describing the same gravity field without any changes to the convergence region.

3 Generating Function for the spherical Bessel function of the first kind

The interior spherical Bessel harmonic gravity field, as derived by Allen et al. [16] and studied by Palmer [17], Herrera-Sucarrat et al. [18], Takahashi and Scheeres [4], Takahashi and Mansell [19, 20], Takahashi et al. [1] is defined below:

$$V^i = \frac{GM^*}{R^*_e}\sum_{l=0}^{\infty}\sum_{n=0}^{\infty}\sum_{m=0}^{n} j_n\left(\frac{\alpha^i_{ln} r}{R^*_e}\right) P_{nm}(\sin\phi)\begin{bmatrix}\cos(m\lambda) \\ \sin(m\lambda)\end{bmatrix}\cdot\begin{bmatrix}\mathscr{A}^i_{lnm} \\ \mathscr{B}^i_{lnm}\end{bmatrix}, \tag{12}$$

where G is the gravitational constant, M^* and R^*_e are the same reference mass/radius as the exterior gravity field, j_n is the spherical Bessel function of the first kind of degree n, α_{ln} is the n-th degree, l-th power scaled eigenvalue of the Helmholtz's equation ($\alpha^i_{ln} = R^*_e k^i_{ln}$) , r is the spacecraft position, P_{nm} is the associated Legendre function of degree n and order m, λ is longitude, and ϕ is latitude in the body-fixed frame. $\mathscr{A}^i_{lnm}$ and $\mathscr{B}^i_{lnm}$ are the interior spherical Bessel coefficients, which are defined in terms of integrals over the mass elements dm' of M as follows:

$$\begin{cases} \mathscr{A}^i_{lnm} &= \dfrac{2(2-\delta_{0m})(2n+1)(n-m)!}{M^*\mathscr{E}^i_n(\alpha^i_{ln})(n+m)!}\displaystyle\int_M j_n\left(\frac{\alpha^i_{ln}r'}{R^*_e}\right)P_{nm}(\sin\phi')\cos(m\lambda')dm', \\ \mathscr{B}^i_{lnm} \overset{m\geq 0}{=} & \dfrac{4(2n+1)(n-m)!}{M^*\mathscr{E}^i_n(\alpha^i_{ln})(n+m)!}\displaystyle\int_M j_n\left(\frac{\alpha^i_{ln}r'}{R^*_e}\right)P_{nm}(\sin\phi')\sin(m\lambda')dm', \end{cases} \tag{13}$$

where $\mathscr{E}^i_q(\alpha^i_{ln}) = \alpha^{i2}_{ln}\left[j_q(\alpha^i_{ln})\right]^2$. The interior spherical Bessel gravity field above (Eq. 12) is derived from the separation of variables of the Poisson's equation [4], which yields the following expression for the density distribution within the Brillouin sphere:

$$\begin{aligned} \rho^i(r,\phi,\lambda) = \frac{M^*}{4\pi R^{*3}_e}\sum_{l=0}^{\infty}\sum_{n=0}^{\infty}\sum_{m=0}^{n}\left(\alpha^{i2}_{ln}j_n\left(\frac{\alpha^i_{ln}r}{R^*_e}\right)\right. \\ \left.\times\ P_{nm}(\sin\phi)\begin{bmatrix}\cos(m\lambda)\\ \sin(m\lambda)\end{bmatrix}\cdot\begin{bmatrix}\mathscr{A}^i_{lnm}\\ \mathscr{B}^i_{lnm}\end{bmatrix}\right). \end{aligned} \tag{14}$$

Similar to the derivation of the exterior gravity field above, we are interested in seeking another method that utilizes the generating function that shed light on the convergence region of the interior spherical Bessel gravity field. Fortunately, we already know the final form of the solution (Eq. 12) and the derivation of the exterior gravity field provides a clue. We turn to the generating function of the spherical Bessel function of the first kind:

$$\frac{cos\left(\sqrt{z^2-2zt}\right)}{z} = \sum_{n=0}^{\infty}\frac{t^n}{n!}j_{n-1}(z). \tag{15}$$

And we immediately hit the roadblock. Eq. 15 is not amenable for substitution in Eq. 4. We could not devise a method to substitute Eq. 15 into Eq. 4 while keeping the generating function for the Legendre polynomial. In other words, the Green's function for the potential does not have a closed form solution with the generating function [21]. This lack of solution for the interior spherical Bessel gravity field via a generating function (the *generating solution*, for short) is puzzling. The generating function is what conferred the exterior gravity field the convergence outside the Brillouin sphere and divergence within. The lack of the generating solution for the interior spherical Bessel gravity field seems to indicate that we have no way of knowing its convergence region had we not derived the exterior gravity field via the generating function already (i.e., Eq. 7).

Another quirk of the interior spherical Bessel gravity field is that the interior spherical Bessel harmonics in Eq. 13 lacks simple scaling of the coefficients via reference radius that we have seen for the exterior spherical harmonics (Eq. 11). Takahashi and Mansell [20] outlined the computation of the interior spherical Bessel harmonics from a homogeneous polyhedral model. It is evident that changing the reference radius would

result in recomputating of the coefficients due to the way the recursive formula is used for the spherical Bessel function of the first kind. Simply put, there is no formula that relates $j_n(x)$ and $j_n(xy)$ via scaling.

As we contemplate on the relationship between the exterior and interior spherical Bessel gravity fields, it is important to be mindful that we have already achived the global mapping of the gravity field anywhere within and around the body. This global mapping enables trajectory propagation anywhere around the body. However, this capability is insufficient for the purpose of navigation. Navigation comprises trajectory design and orbit determination (OD), and both elements require the computation of the sensitivity matrices (e.g., state transition matrix). For example, we model the gravity field outside the Brillouin sphere with the exterior spherical harmonics (C^e_{nm}, S^e_{nm}), and that inside with the interior spherical Bessel harmonics ($\mathscr{A}^i_{lnm}$, $\mathscr{B}^i_{lnm}$). As the spacecraft penetrates and comes in/out of the Brillouin sphere, the nominal trajectory computation can be performed without any difficulty. However, the question remains: how do the sensitivities/uncertainies of the exterior spherical harmonics map to the spacecraft state and other parameters that influence the target parameters (e.g., the rotational state of the body) and measurements when the spacecraft penetrates from outside to inside the Brillouin sphere? Upon crossing the boundary the exterior gravity field is no longer a valid representation, invalidating the computation of the sensitivity matrices. And similarly, how do the sensitivities/uncertainies of the interior spherical Bessel harmonics map to other parameters when the spacecraft escapes from inside to the outside of the Brillouin sphere? As the spacecraft travels in and out of the Brillouin sphere, we lose the means to map the sensitivity of those harmonic coefficients to the state and measurements. This is not only troublesome for the trajectory design/OD applications, but it also strikes as odd; the gravity field does not know that it is modeled as spherical harmonics, and it is oblivious to the limitations of the spherical harmonics representations. The sensitivity of the gravity field should be continuous.

What we know, however, is that the interior spherical Bessel gravity field needs to make a smooth, continuous transition from the exterior gravity field at the Brillouin sphere. Based on the lack of generating solution and lack of simple scaling of the coefficients via reference radii, we suspect that the absence of the generating solution for the interior spherical Bessel gravity field is due to the arbitrary choice of the reference radius we can make for the exterior gravity field. That is, the interior spherical Bessel gravity field is only required to match the potential and acceleration of the exterior gravity field at the reference sphere, and we can arbitrarily pick such a sphere. Because the exterior gravity field is obtained by solving for the Laplace's equation, this scaled Brillouin sphere is any sphere equal to or larger than the physical Brillouin sphere. If this hypothesis is true, then the interior spherical Bessel gravity field converges within any arbitrarily scaled Brillouin sphere. The continuity constraints on the potential and acceleration at the scaled Brillouin sphere results in the same eigenvalues α^i_{ln} [1, 4, 20], preserving all of the expressions/properties of the interior spherical Bessel gravity field.

In the next few sections we derive expressions for the scaled interior spherical Bessel gravity field. Note that, at the moment of derivation we do not know if this is a valid

attempt mathematically. It is only an ansatz. In later sections we numerically verify the results to conclude that those derivations were indeed correct. If the analytical proof is desired, we invite the readers to join our effort. However, for astrodynamics applications, it only suffices to have numerical validations.

4 Interior spherical Bessel harmonics for a homogeneous sphere with scaled reference radius

In this section we compute the interior spherical Bessel harmonics for a homogeneous sphere with a scaled radius. The same was done by Takahashi and Mansell [19] and Takahashi et al. [1] using the physical Brillouin radius as the reference radius. We revisit their formulation for the scaled reference radius.

We define R_e^* as the physical Brillouin radius (as before) and $\check{R}_e^*$ as the scaled reference radius. For convenience, we define the reference radius ratio $\tilde{R}_e \leq 1$:

$$\tilde{R}_e = \frac{R_e^*}{\check{R}_e^*}. \tag{16}$$

From Takahashi and Mansell [20], we have the expression for the interior spherical Bessel harmonics for a homogeneous body. The divergence theorem is applied to reduce the volume integral in Eq. 13 into the surface integral:

$$\begin{bmatrix} \mathscr{A}_{lnm}^i \\ \mathscr{B}_{lnm}^i \end{bmatrix} = \frac{\rho_0}{M^*} \iint_S F_{r'} \hat{r'} \cdot \hat{n} dS, \tag{17}$$

where ρ_0 is the homogeneous density of the body. $F_{r'}$ is defined as

$$\begin{aligned} F_{r'} = & \frac{2(2-\delta_{0m})(2n+1)(n-m)!}{\mathscr{E}_n^i(\alpha_{ln}^i)(n+m)!} \left(\frac{\alpha_{ln}^i}{R_e^*}\right)^{-3} \\ & \times \frac{P_{nm}(\sin\phi')}{(r')^2} \left[I_{n2}\left(\frac{\alpha_{ln}^i r'}{R_e^*}\right) - I_{n2}(0) \right] \begin{bmatrix} \cos(m\lambda') \\ \sin(m\lambda') \end{bmatrix}, \end{aligned} \tag{18}$$

where r', ϕ', and λ' are with respect to the coordinate of a point on the surface and $I_{nq}(x)$ is defined as follows:

$$I_{nq}(x) = \int x^q j_n(x) dx. \tag{19}$$

In Eq. 17, we only need to concern ourselves with the top facet facing outward due to the alternating signs of $\hat{n}$ for the side facets. Note that $I_{n2}(0)$ is only non-zero for $n = 1$. For the interior spherical Bessel harmonics with scaled reference radius, all that is needed is to replace R_e^* with $\check{R}_e^*$ in Eq. 18 to define $\check{F}_{r'}$. Everything else is the same as before. That is,

$$\check{F}_{r'} = \frac{2(2-\delta_{0m})(2n+1)(n-m)!}{\mathscr{E}_n^i(\alpha_{ln}^i)(n+m)!}\left(\frac{\alpha_{ln}^i}{\check{R}_e^*}\right)^{-3} \times \frac{P_{nm}(\sin\phi')}{(r')^2}\left[I_{n2}\left(\frac{\alpha_{ln}^i r'}{\check{R}_e^*}\right) - I_{n2}(0)\right]\begin{bmatrix}\cos(m\lambda') \\ \\ \sin(m\lambda')\end{bmatrix}, \tag{20}$$

For a homogeneous sphere the expression in Eq. 20 greatly simplies as well as Eq. 17. In particular, we only need to consider the zeroth degree and zeroth order coefficients due to the orthogonality of the surface spherical harmonics (Takahashi and Mansell [19]). Then, remembering that the limit of the mass integral still ends at the physical Brillouin radius R_e^* even with the scaled reference radius, the scaled interior spherical Bessel harmonics for a homogeneous sphere becomes

$$\begin{bmatrix}\check{\mathscr{A}}_{l00}^i \\ \check{\mathscr{B}}_{l00}^i\end{bmatrix} = \frac{\rho_0}{M^*} 4\pi \left(R_e^*\right)^2 \check{F}_{l00,R_e^*}, \tag{21}$$

where

$$\check{F}_{l00,R_e^*} = 2\left(\frac{\alpha_{l0}^i}{\check{R}_e^*}\right)^{-3} \frac{1}{(R_e^*)^2} I_{02}\left(\alpha_{l0}^i \tilde{R}_e\right)\begin{bmatrix}1 \\ \\ 0\end{bmatrix}. \tag{22}$$

Note that we substituted $\mathscr{E}_0^i(\alpha_{l0}^i) = 1$. Then, by substituting the total mass ($M^* = 4\pi(R_e^*)^3\rho_0/3$) in Eq. 21, we get

$$\begin{bmatrix}\check{\mathscr{A}}_{l00}^i \\ \check{\mathscr{B}}_{l00}^i\end{bmatrix} = 6\left(\alpha_{l0}^i \tilde{R}_e\right)^{-3} I_{02}\left(\alpha_{l0}^i \tilde{R}_e\right)\begin{bmatrix}1 \\ \\ 0\end{bmatrix}. \tag{23}$$

As expected, the coefficients $\check{\mathscr{A}}_{l00}^i$ do not depend on the reference mass but do on the ratio of the reference radii. The analytical form of $I_{02}(x)$ is simple to compute and is given as follows:

$$I_{02}(x) = \sin(x) - x\cos(x). \tag{24}$$

Thus, the interior spherical Bessel harmonics are uniquely computed for a homogeneous sphere once the ratio of the physical Brillouin radius to the scaled reference radius is defined. The resultant potential expression is below:

$$\check{V}_{sphere}^i = \frac{GM^*}{\check{R}_e^*}\sum_{l=0}^{\infty} j_0\left(\frac{\alpha_{l0}^i r}{\check{R}_e^*}\right)\check{\mathscr{A}}_{l00}^i = \frac{6GM^*}{\check{R}_e^*\tilde{R}_e^3}\sum_{l=0}^{\infty} j_0\left(\frac{\alpha_{l0}^i r}{\check{R}_e^*}\right)\left(\alpha_{l0}^i\right)^{-3} I_{02}\left(\alpha_{l0}^i \tilde{R}_e\right) \tag{25}$$

We also have the density distribution as follows:

$$\check{\rho}^i_{sphere}(r) = \frac{M^*}{4\pi \check{R}^{*3}_e} \sum_{l=0}^{\infty} \alpha^{i2}_{l0} j_0 \left(\frac{\alpha^i_{l0} r}{\check{R}^*_e} \right) \check{\mathscr{A}}^i_{l00} = 2\rho_0 \sum_{l=0}^{\infty} j_0 \left(\frac{\alpha^i_{l0} r}{\check{R}^*_e} \right) \left(\alpha^i_{l0} \right)^{-1} I_{02} \left(\alpha^i_{l0} \tilde{R}_e \right). \tag{26}$$

Using the density definition in Eq. 26, we can compute the mass within a certain sphere of radius $r \leq \check{R}^*_e$.

$$M_{sphere}(r) = \int_V \rho^i dV = \frac{6M^*}{\tilde{R}^3_e} \sum_{l=0}^{\infty} \left(\alpha^i_{l0} \right)^{-4} I_{02} \left(\frac{\alpha^i_{l0} r}{\check{R}^*_e} \right) I_{02} \left(\alpha^i_{l0} \tilde{R}_e \right). \tag{27}$$

Therefore, at the physical Brillouin sphere and the scaled Brillouin sphere, we have

$$M_{sphere}(R^*_e) = \frac{6M^*}{\tilde{R}^3_e} \sum_{l=0}^{\infty} \left(\alpha^i_{l0} \right)^{-4} \left[I_{02} \left(\alpha^i_{l0} \tilde{R}_e \right) \right]^2, \tag{28}$$

$$M_{sphere}(\check{R}^*_e) = \frac{6M^*}{\tilde{R}^3_e} \sum_{l=0}^{\infty} (-1)^l \left(\alpha^i_{l0} \right)^{-4} I_{02} \left(\alpha^i_{l0} \tilde{R}_e \right), \tag{29}$$

where we substituted the analytical expression for the zeroth-degree eigenvalue: $\alpha^i_{l0} = (2l+1)\pi/2$. This yields $I_{02}(\alpha^i_{l0}) = \sin(\alpha^i_{l0}) = (-1)^l$.

It is important to remark here that because we have distributed the mass within the scaled Brillouin sphere, we expect $M_{sphere}(\check{R}^*_e) = M^*$. To prove, we first invoke the harmonic constraint equations [1, 4, 18, 20]:

$$\begin{cases} C^e_{nm} = \sum_{l=l^*}^{\infty} j_n(\alpha^i_{ln}) \mathscr{A}^i_{lnm}, \\ \\ S^e_{nm} = \sum_{l=l^*}^{\infty} j_n(\alpha^i_{ln}) \mathscr{B}^i_{lnm}, \end{cases} \tag{30}$$

where

$$l^* = \begin{cases} 0 \text{ , for } n = 0, 1, \\ \\ 1 \text{ , for } \quad n > 1. \end{cases} \tag{31}$$

The above equations are for the original coefficients that used the physical Brillouin radius as the reference radius. For the scaled coefficients, we have

$$\begin{cases} \check{C}^e_{nm} = \left(\tilde{R}_e\right)^n C^e_{nm} = \sum_{l=l^*}^{\infty} j_n(\alpha^i_{ln}) \check{\mathscr{A}}^i_{lnm}, \\ \check{S}^e_{nm} = \left(\tilde{R}_e\right)^n S^e_{nm} = \sum_{l=l^*}^{\infty} j_n(\alpha^i_{ln}) \check{\mathscr{B}}^i_{lnm}. \end{cases} \tag{32}$$

Even after the change of the reference radius, $\check{C}^e_{00} = 1$. Thus, we get

$$\check{C}^e_{00} = 1 = \sum_{l=0}^{\infty} j_0(\alpha^i_{l0}) \check{\mathscr{A}}^i_{l00} = \frac{6}{\tilde{R}^3_e} \sum_{l=0}^{\infty} \left(\alpha^i_{l0}\right)^{-3} j_0(\alpha^i_{l0}) I_{02}\left(\alpha^i_{l0}\tilde{R}_e\right), \tag{33}$$

which yields

$$M_{sphere}(\check{R}^*_e) = \frac{6M^*}{\tilde{R}^3_e} \sum_{l=0}^{\infty} \left(\alpha^i_{l0}\right)^{-4} \sin\left(\alpha^i_{l0}\right) I_{02}\left(\alpha^i_{l0}\tilde{R}_e\right) = M^*. \tag{34}$$

We have recovered the total mass at the scaled Brillouin sphere as expected. An important concept that we will explore later is how much mass is contained within a sphere of radius r. We call it the spherical mass fraction and define it as follows:

$$\tilde{m}_{sphere}(r) = \frac{M_{sphere}(r)}{M^*}. \tag{35}$$

We will numerically prove Eq. 27 later by computing the mass fraction in Eq. 35, validating the scaled interior spherical Bessel harmonics we derived in Eq. 23. Another numerical proof is also given in the next section when deriving the special infinite series for the scaled interior spherical Bessel harmonics.

4.1 Sphecial functions derived from the interior spherical Bessel harmonics for a homogeneous sphere with scaled reference radius

In Takahashi et al. [1], they derived various relationships between the interior spherical Bessel harmonics, Riemann zeta function, and other special functions. We are curious to see how they modify for the scaled harmonics.

4.1.1 Potential

First, we consider the potential at $r = \check{R}^*_e$ (i.e., at the scaled reference radius). This results in the boundary condition in Eq. 33. By direct substitution, we get

$$\sum_{l=0}^{\infty} \frac{(-1)^l}{(2l+1)^4} I_{02}\left(\alpha_{l0}^i \tilde{R}_e\right) = \frac{\pi^4}{96} \tilde{R}_e^3. \tag{36}$$

For the original formulation where $\tilde{R}_e = 1$, $I_{02}\left(\alpha_{l0}^i \tilde{R}_e\right)$ simplifies to $(-1)^l$, yielding $\zeta(2)$ without the sieving of a factor 2 as discussed in Takahashi et al., [1]. As a reminder, Riemann zeta function $\zeta(s)$ is defined as follows:

$$\zeta(s) = \sum_{n=1}^{\infty} \frac{1}{n^s} = 1 + \frac{1}{2^s} + \frac{1}{3^s} + \frac{1}{4^s} + \cdots, \tag{37}$$

where $\Re(s) > 1$. For a general case with $\tilde{R}_e < 1$, $I_{02}\left(\alpha_{l0}^i \tilde{R}_e\right)$ (Eq. 24) does not simplify, so we left it as is. Eq. 36 is interesting because the asymptote is scaled by the factor $\tilde{R}_e^3$ relative to the original derivation to capture the fractional change in the volume of the Brillouin sphere. When $\tilde{R}_e \to 0$, we could not obtain an interesting convergence property from Eq. 36, except that both sides of the equation tend to zero [2].

At $r = R_e^*$ (i.e., at the physical Brillouin radius), we get

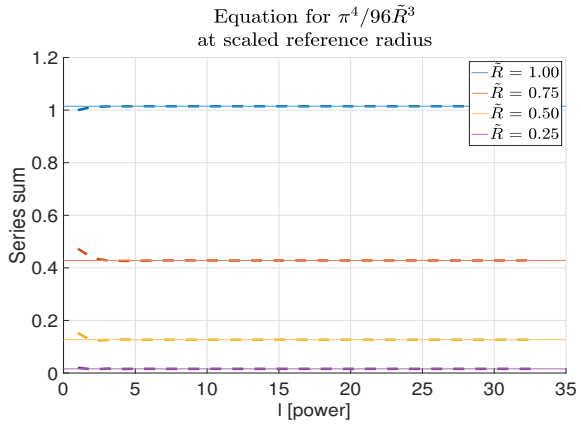
$$\begin{aligned} \check{V}_{sphere}^i(R_e^*) = \frac{GM^*}{\check{R}_e^*} \sum_{l=0}^{\infty} j_0\left(\frac{\alpha_{l0}^i R_e^*}{\check{R}_e^*}\right) \check{\mathscr{A}}_{l00}^i = \frac{GM^*}{R_e^*} \\ \Rightarrow \qquad \sum_{l=0}^{\infty} \frac{\sin(\alpha_{l0}^i \tilde{R}_e) I_{02}\left(\alpha_{l0}^i \tilde{R}_e\right)}{(2l+1)^4} = \frac{\pi^4}{96} \tilde{R}_e^3. \end{aligned} \tag{38}$$

Similarly, at $r = 0$ (i.e., at the coordinate center),

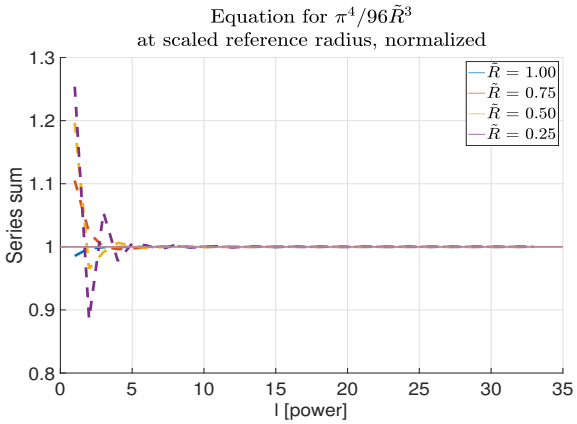
$$\begin{aligned} \check{V}_{sphere}^i(0) = \frac{GM^*}{\check{R}_e^*} \sum_{l=0}^{\infty} j_0(0) \check{\mathscr{A}}_{l00}^i = \frac{GM^*}{\check{R}_e^*} \sum_{l=0}^{\infty} \check{\mathscr{A}}_{l00}^i = \frac{3GM^*}{2R_e^*} \\ \Rightarrow \qquad \sum_{l=0}^{\infty} \frac{I_{02}\left(\alpha_{l0}^i \tilde{R}_e\right)}{(2l+1)^3} = \frac{\pi^3}{32} \tilde{R}_e^2. \end{aligned} \tag{39}$$

[2] The R.H.S of the equation approaches zero faster than the L.H.S. This hints that the infinitely large scaled Brillouin radius (i.e., infinitesimal $\tilde{R}_e$) is not only unrealistic but also not mathematically possible.

Eqs. 36 through 39 are numerically verified in Figs. 3 through 5. The left plots show the series sum, and the right plots show the normalized series sum (i.e., the series are normalized to sum to 1). This is the first validation of the scaled interior spherical Bessel harmonics in Equation 23. Had they not been valid, the infinite series in Eqs. 36 through 39 would have diverged as we added more terms (i.e., more powers l).

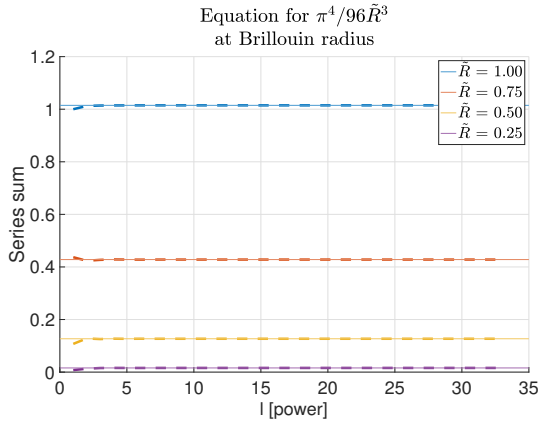


(a) Eq. 36: actual sum.

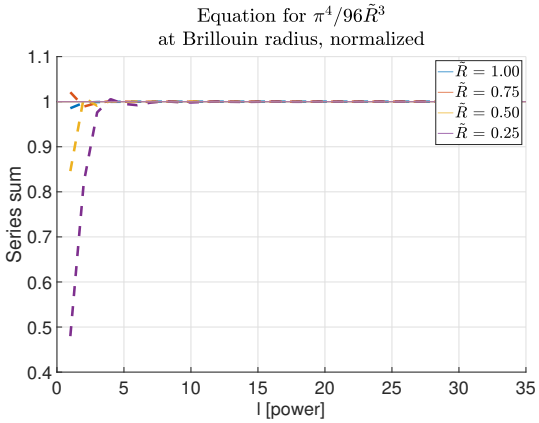


(b) Eq. 36: normalized sum.

Fig. 3: Eq. 36 with $\tilde{R}_e = 1$, 0.75, 0.5, and 0.25. $l_{max} = 32$.

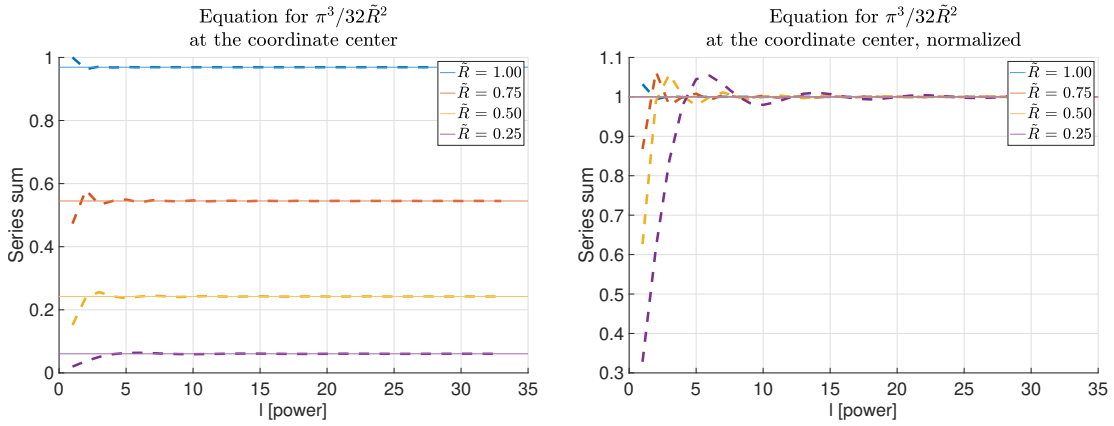


(a) Eq. 38: actual sum.



(b) Eq. 38: normalized sum.

Fig. 4: Eq. 38 with $\tilde{R}_e = 1$, 0.75, 0.5, and 0.25. $l_{max} = 32$.



(a) Eq. 39: actual sum.

(b) Eq. 39: normalized sum.

Fig. 5: Eq. 39 with $\tilde{R}_e = 1$, 0.75, 0.5, and 0.25. $l_{max} = 32$.

4.1.2 Density

For the density, we have derived a few special functions in Takahashi et al. [1]. For the unscaled reference radius, we already know that the density at the Brillouin radius is the homogeneous density ρ_0 (i.e., $\check{\rho}^i_{sphere}(\check{R}^*_e) = \rho_0$ when $\tilde{R}_e = 1$). For the scaled reference radius, we consider the case where $\tilde{R}_e \neq 1$. In this case, there is no physical mass at this reference radius, so we should obtain $\check{\rho}^i_{sphere}(\check{R}^*_e) = 0$:

$$\begin{aligned} \check{\rho}^i_{sphere}(\check{R}^*_e) &= 2\rho_0 \sum_{l=0}^{\infty} j_0\left(\alpha^i_{l0}\right)\left(\alpha^i_{l0}\right)^{-1} I_{02}\left(\alpha^i_{l0}\tilde{R}_e\right) = 0 \\ \Rightarrow \qquad & \sum_{l=0}^{\infty} \frac{(-1)^l I_{02}\left(\alpha^i_{l0}\tilde{R}_e\right)}{(2l+1)^2} = 0 \end{aligned} \tag{40}$$

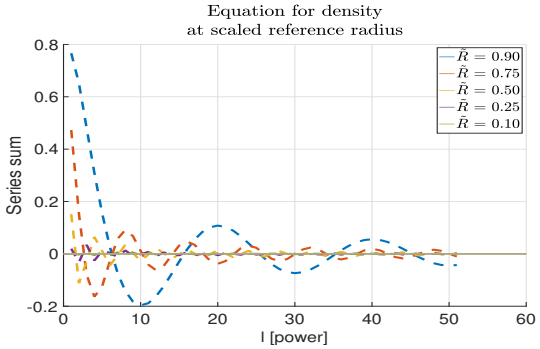
At $r = R^*_e$, we observe an interesting phenomenon. Rather than converging to the actual density ρ_0, we observe that the density converges to the average of the densities inside and outside the physical body. That is, $\check{\rho}^i_{sphere}(R^*_e) = \rho_0/2$ when $\tilde{R}_e \neq 1$:

$$\begin{aligned} \breve{\rho}^i_{sphere}(R^*_e) &= 2\rho_0 \sum_{l=0}^{\infty} j_0\left(\alpha^i_{l0}\tilde{R}_e\right)\left(\alpha^i_{l0}\right)^{-1} I_{02}\left(\alpha^i_{l0}\tilde{R}_e\right) = \frac{\rho_0}{2} \\ \Rightarrow \quad & \sum_{l=0}^{\infty} \frac{\sin(\alpha^i_{l0}\tilde{R}_e) I_{02}\left(\alpha^i_{l0}\tilde{R}_e\right)}{(2l+1)^2} = \frac{\pi^2}{16}\tilde{R}_e \end{aligned} \tag{41}$$

This is a classical Gibb's phenomenon. The sharp transition from the non-zero density to zero is attained in the averaged sense. At $r = 0$, we expect $\breve{\rho}^i_{sphere}(0) = \rho_0$, which results in the following:

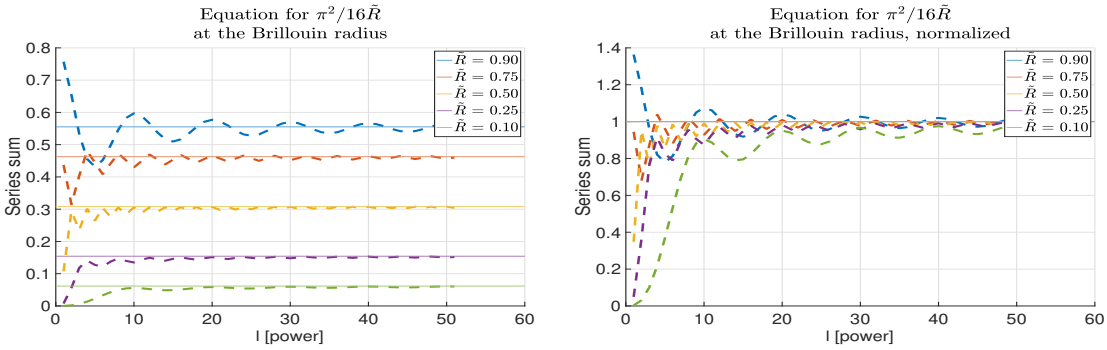
$$\begin{aligned} \breve{\rho}^i_{sphere}(0) &= 2\rho_0 \sum_{l=0}^{\infty} j_0(0)\left(\alpha^i_{l0}\right)^{-1} I_{02}\left(\alpha^i_{l0}\tilde{R}_e\right) = \rho_0 \\ \Rightarrow \quad & \sum_{l=0}^{\infty} \frac{I_{02}\left(\alpha^i_{l0}\tilde{R}_e\right)}{2l+1} = \frac{\pi}{4} \qquad \underline{\text{this equation is not correct}} \end{aligned} \tag{42}$$

However, Eq. 42 is not substantiated numerically as we will see shortly. We present the numerical results for Eqs. 40 through 42 in Figs 6 through 8. Fig. 6 shows that the density tends to zero at the scaled reference radius according to Eq. 40. Eq. 41 tends to the average density at the Brillouin radius when $\tilde{R}_e \neq 1$, and Eq. 42 simply oscillates rather than reaching convergence. The limits of Eqs. 41 and 42 need a more thorough analysis but it is omitted from this work. When understood properly, these two equations may aid in conferring physical meanings to the scaling of the Brillouin radius. Despite the shortcomings of the analysis, it is important to note that there is no sign of divergence in any of Eqs. 40 through 42, supporting the hypothesis that it is possible to expand the convergence region of the interior spherical Bessel gravity field.



(a) Eq. 40 value.

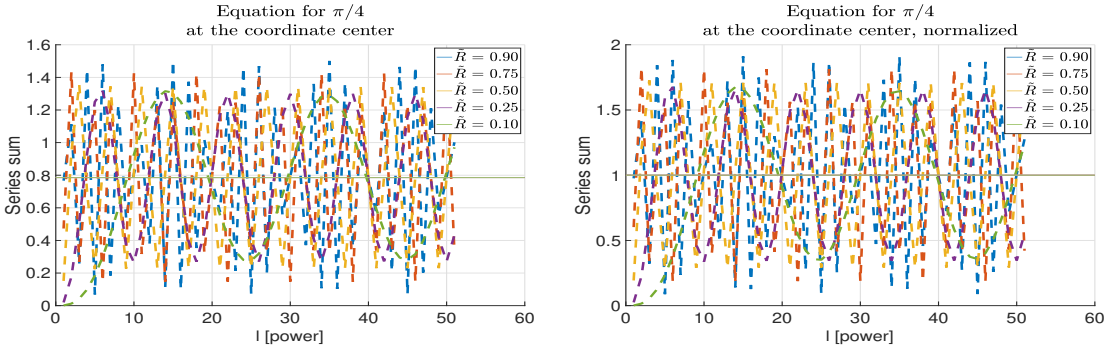
Fig. 6: Eq. 40 with $\tilde{R}_e = 0.9$, 0.75, 0.5, 0.25, and 0.10. $l_{max} = 50$.



(a) Eq. 41 value.

(b) Eq. 41 normalized.

Fig. 7: Eq. 41 with $\tilde{R}_e = 0.9$, 0.75, 0.5, 0.25, and 0.10. $l_{max} = 50$.



(a) Eq. 42 value.

(b) Eq. 42 normalized.

Fig. 8: Eq. 42 with $\tilde{R}_e = 0.9$, 0.75, 0.5, 0.25, and 0.10. $l_{max} = 50$.

5 Interior spherical Bessel harmonics for a homogeneous polyhedron with a scaled reference radius

For a general polyhedron with homogeneous density, we can leverage the techniques by Takahashi and Mansell [20] to compute the interior spherical Bessel harmonics. The only change we need to make is to use Eq. 20 instead of Eq. 18. We approximate the surface integral in Eq. 17 by computing $\check{F}_{r'}$ at center of the top facet and multiplying it by the facet area. We sum over all facets to obtain the coefficients.

Similarly to the homogeneous sphere with the scaled reference radius, we are interested in computing how much mass is allocated within a spere of radius r for a general shape model. Recalling to replace the original quantities with the scaled quantities in Eq. 14 for the density expression, we get

$$M_{sphere}(r) = \int_V \check{\rho}^i dV \quad = M^* \sum_{l=0}^{\infty} \frac{1}{\alpha_{l0}^i} I_{02}\left(\frac{\alpha_{l0}^i r}{\check{R}_e^*}\right) \check{\mathscr{A}}_{l00}^i \tag{43}$$

where we used the orthogonal property of the surface spherical harmonics (see the proof in Eq. A1). Thus, the general form of the spherical mass fraction is as follows:

$$\tilde{m}_{sphere}(r) = \frac{M_{sphere}(r)}{M^*} = \sum_{l=0}^{\infty} \frac{1}{\alpha_{l0}^i} I_{02}\left(\frac{\alpha_{l0}^i r}{\check{R}_e^*}\right) \check{\mathscr{A}}_{l00}^i \tag{44}$$

Another quantity of interest is how much of the total mass is within the scaled shape model (s) (see the proof in Eq. A2).

$$\begin{aligned} M_{shape}(s) = \frac{M^*}{4\pi} \sum_{f \in facets} \frac{\hat{\bar{r}}_f \cdot \hat{n}_f \bar{S}_f}{\bar{r}_f^2} \left(\sum_{l=0}^{\infty} \sum_{n=0}^{\infty} \frac{1}{\alpha_{ln}^i} \left[I_{n2}\left(\frac{\alpha_{ln}^i \bar{r}_f}{\check{R}_e^*}\right) - I_{n2}(0) \right] \right. \\ \left. \times \left(\sum_{m=0}^{n} P_{nm}(\sin\bar{\phi}_f) \begin{bmatrix} \cos(m\bar{\lambda}_f) \\ \sin(m\bar{\lambda}_f) \end{bmatrix} \cdot \begin{bmatrix} \check{\mathscr{A}}_{lnm}^i \\ \check{\mathscr{B}}_{lnm}^i \end{bmatrix} \right) \right) \end{aligned} \tag{45}$$

where the overbar indicates the quantities at the center of the top facet and we used the same reduction of the volume integral into the surface integral assuming a radial function that allowed us to derive Eqs. 17 and 18 (see Takahashi and Mansell [20] for details). The only difference this time is that we did not have to assume a homogeneous density distribution. The volume integral appears by definition. Because the heterogeneity in density distribution is baked into the coefficients $\check{\mathscr{A}}_{lnm}^i$ and $\check{\mathscr{B}}_{lnm}^i$, the formulation in Eq. 45 works for any general body. It is interesting to note that the scalar multiplier within the facet summation $\hat{\bar{r}}_f \cdot \hat{n}_f \bar{S}_f / \bar{r}_f^2$ is the same for both the scaled/unscaled shape model, and so are $\bar{\phi}_f$ and $\bar{\lambda}_f$. Thus, the only component that differentiates the scaled/unscaled model is $\bar{r}_f$ inside I_{n2}. From Eq. 45, we can define the scaled shape mass fraction as follows:

$$\tilde{m}_{shape} = \frac{M_{shape}(s)}{M^*} \tag{46}$$

6 Evaluation of the scaled interior spherical Bessel harmonics - Mass, Potential, and Acceleration -

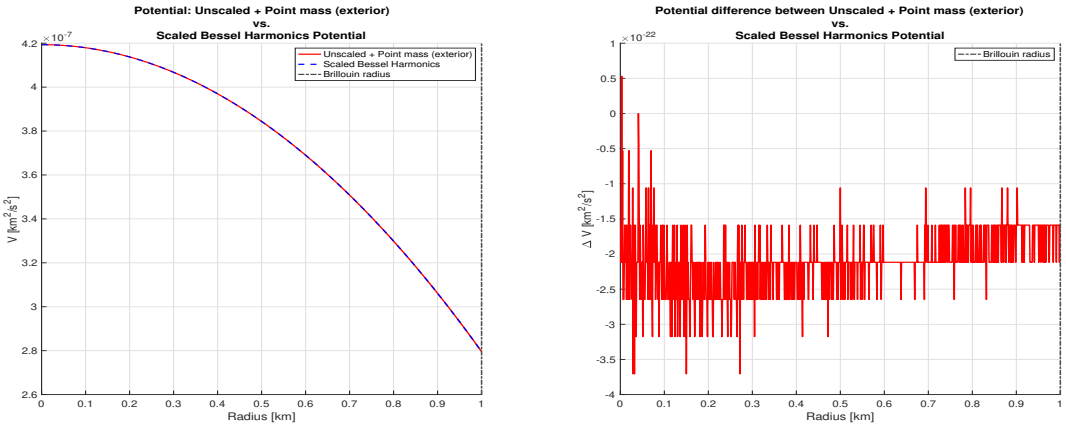
In the following sections, we evaluate our hypothesis that the interior spherical Bessel gravity field can expand its convergence by comparing the scaled interior spherical Bessel gravity field against the known truth model. We will look at two bodies: a homogeneous sphere and a homogeneous Phobos. First, we present the results for a homogeneous sphere.

6.1 Scaled interior spherical Bessel harmonics for a homogeneous sphere

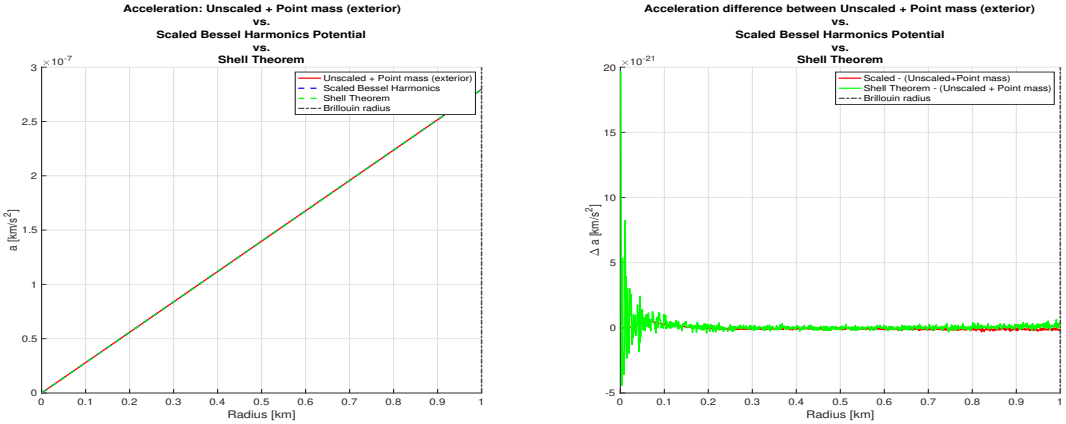
Our baseline model is the homogeneous unit sphere with unit density. That is, $R_e^* = 1$ $[km]$ and $\rho_0 = 1$ $[g/cm^3]$. In the next set of plots, we present the potential/acceleration/density values from the three models below:

- Unscaled + point mass (red): Inside the physical Brillouin sphere, this model computes the value based on the original, unscaled interior spherical Bessel harmonics. Outside the sphere, the value is computed based on the point mass gravity field. This is the model to be used had it not been possible to expand the convergence region of the interior spherical Bessel gravity field.
- Scaled Bessel harmonics (blue): This model computes the value based on the scaled interior spherical Bessel harmonics anywhere within the scaled reference radius. This model should be identical to the first model if the convergence region can be expanded.
- Shell Theorem (green): This model computes the mass fraction based on Eq. 27, and computes the value based on that mass fraction using the Shell Theorem (i.e., point mass gravity of the mass beneath). If the convergence region can be expanded, our mass fraction should correctly yield the mass beneath the evaluation point and the same gravity field as the first. While the processes are different, the second and the third models are identical in their formulation.

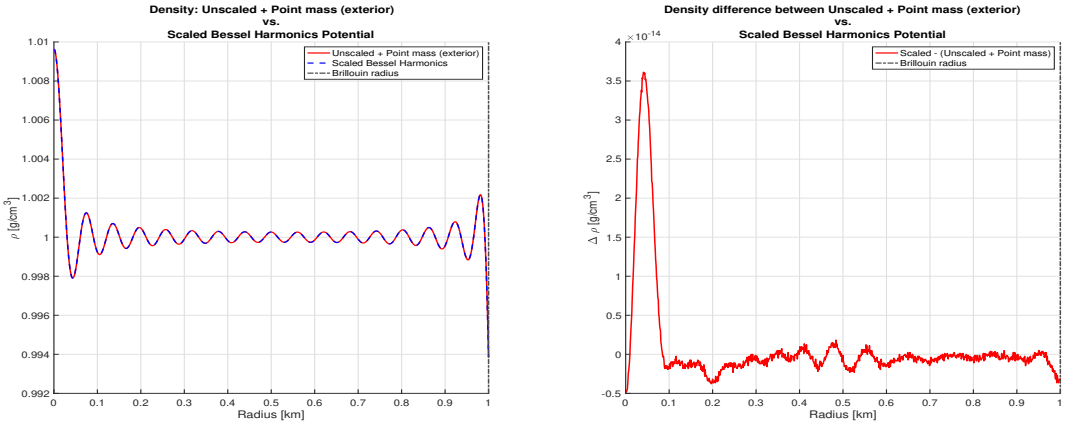
We first present the results for the unscaled harmonics. In this case the scaled and unscaled harmonics are identical ($\tilde{R}_e = 1$, the upper bound of the reference radius ratio), and we expect that the potential, acceleration, and density distribution is nearly perfectly modeled by the interior spherical Bessel gravity field as presented in Takahashi et al. [1]. Fig. 9 shows these comparisons for $l_{max} = 32$, where the values are on the left and the difference are on the right. As expected, they agree with numerical precision. For the density comparisons, the differences are between the scaled and unscaled interior spherical Bessel gravity models (i.e., not relative to the truth value of ρ_0).



(a) Potential comparison (value: left, delta: right).



(b) Acceleration comparison (value: left, delta: right).



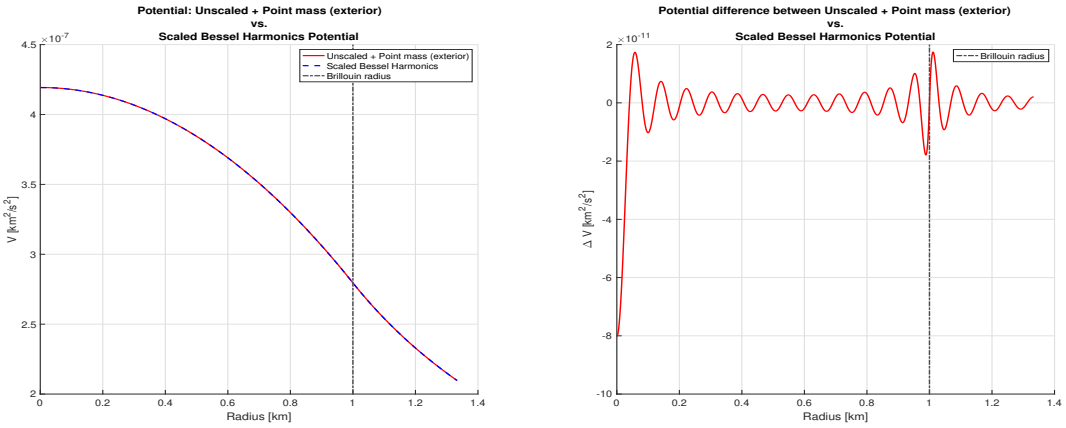
(c) Density comparison (value: left, delta: right).

Fig. 9: Potential, acceleration, and density comparisons for a homogeneous unit sphere with $\tilde{R}_e = 1$, $l_{max} = 32$. The values are shown on the left and the differences are shown on the right.

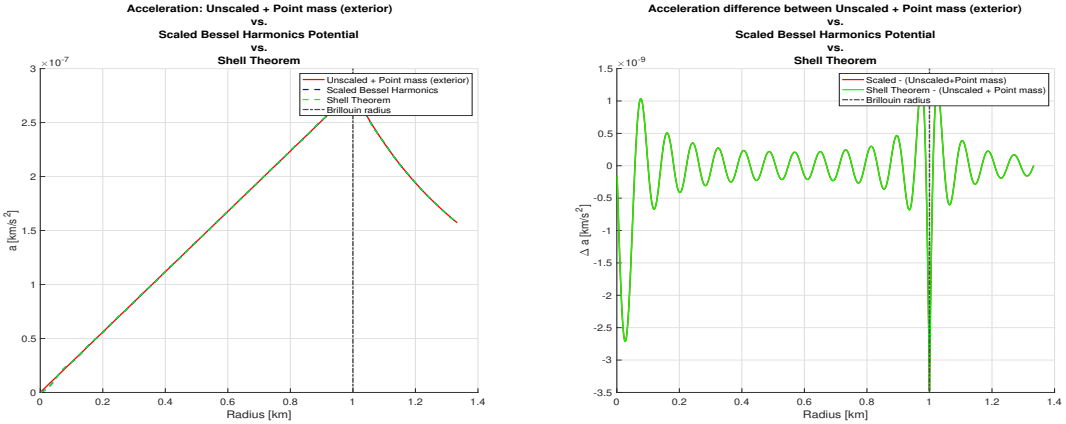
Fig. 10 shows the same plots for $\tilde{R}_e = 0.75$. In this case the scaled reference radius is larger than the physical Brillouin radius, creating a void between the two spheres. Because the original unscaled harmonics only work within the physical Brillouin sphere, the potential and acceleration outside the physical Brillouin sphere are computed from the point mass gravity field for the red lines. The blue lines are computed from the scaled harmonics throughout the scaled Brillouin sphere (Eq. 23). The Shell Theorem acceleration outside the physical Brillouin sphere is computed from the point mass gravity field (same as the red line). The results in Fig. 10 are astounding. Not only are the potential and acceleration perfectly modeled with the scaled harmonics (blue lines), but the density profile drops to zero outside the physical Brillouin sphere, denoted as the vertical dashed black lines. This result is particularly remarkable, because the scaled harmonics in Eq. 23 are constants after all. That is, it is not immediately clear that the zero crossing must occur at the physical boundary of the body. In other words, Eq. 26 appears to make a smooth, continuous curve for $r \geq R_e^*$ (in the void region), and the sudden drop of density to zero across the physical Brillouin sphere is not immediately clear from the expression.

These results numerically corroborates our hypothesis that the convergence region of the interior spherical Bessel gravity field can be arbitrarily made larger than the physical Brillouin sphere. What is particularly amazing is that it does so by dropping the density to nearly zero outside the physical Brillouin sphere, save for the oscillation due to $j_n(x)$ being a function of sine and cosine. This further corroborates our statement from the previous publication that the interior spherical Bessel gravity field is a general form of the Sir Isaac Newton's Shell Theorem (Takahashi et al. [1]). At each evaluation point, the outer shells of nearly zero density contribute no net acceleration to the field point.

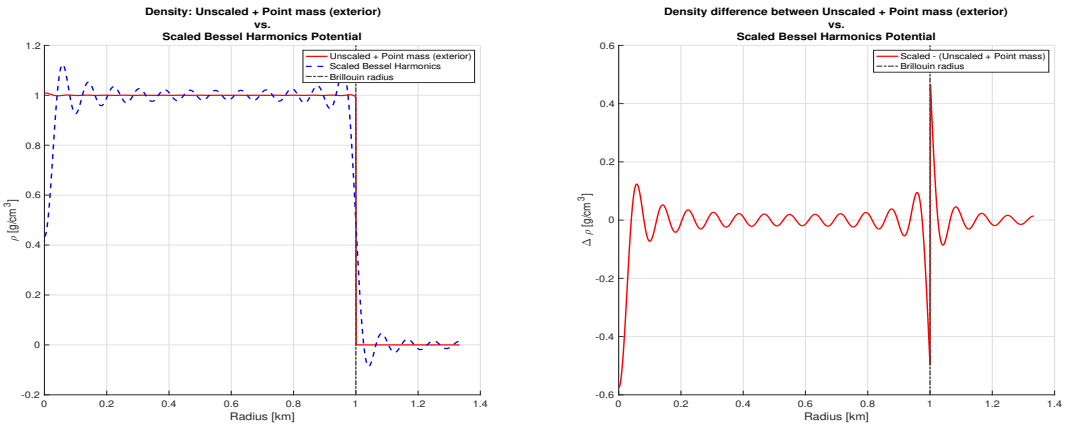
The quantative/qualitative results do not change for a smaller reference radius ratio ($\tilde{R}_e$). We show the same potential, acceleration, and density comparisons when the reference radius is twice and four times larger than the physical Brillouin sphere ($\tilde{R}_e = 0.5$ and 0.25) in Appendix (Figs. C2 and D3). Recall that, had we done the same analysis for the exterior gravity field (i.e., compute the potential/acceleration errors at 0.75, 0.50, and 0.25 of the physical Brillouin sphere), the errors become exponentially high due to divergence. The fact that the potential/acceleration values are even *bounded* is a clear indication that the we can expand the convergence region of the interior spherical Bessel harmonic gravity field by scaling the reference radius.



(a) Potential comparison (value: left, delta: right).



(b) Acceleration comparison (value: left, delta: right).



(c) Density comparison (value: left, delta: right).

Fig. 10: Potential, acceleration, and density comparisons for a homogeneous unit sphere with $\tilde{R}_e = 0.75$, $l_{max} = 32$. The values are shown on the left and the differences are shown on the right.

Next, we plot the spherical mass fraction. We provide the line plot on the left and the contour on the right, representing the concentric spheres of the same spherical mass fraction. The radius ratio on the axes represent the ratio of the physical Brillouin radius to the scaled reference radius. This puts the physical Brillouin sphere at the same value as the reference radius ratio ($\tilde{R}_e$), facilitating the visual interpretation. The first result is for $\tilde{R}_e = 1.0$, where the physical and scaled reference radii are the same. It it presented in Fig. 11. We increased the maximum power l_{max} to 50, but essentially the same results are obtained with l_{max} of 32.

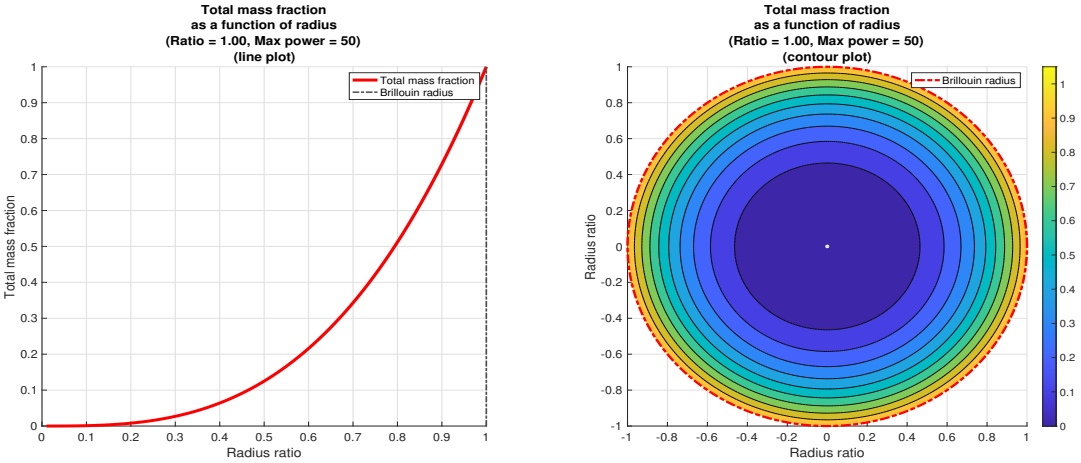


Fig. 11: Spherical mass fraction ($\tilde{m}_{sphere}(r)$) as a function of radius (left) and in contour (right) for $\tilde{R}_e = 1.0$, $l_{max} = 50$.

As expected, the spherical mass fraction monotonically increases as a cubic function and 100% of the total mass is reached at the Brillouin radius. Fig. 12 shows the same plots for $\tilde{R}_e = 0.75$. As clearly shown, nearly 100%, if not precisely 100%, of mass is within the physical Brillouin sphere. The void region is simply the oscillation due to the near-zero density profile in Fig. 10. This reinforces our understanding that the interior spherical Bessel gravity field is the general form of the Shell Theorem. The plots for $\tilde{R}_e = 0.50$ and 0.25 are shown in the Appendix. It is truly amazing that 100% of the total mass actually resides within the physical Brillouin sphere even when the scaled reference radius is four times larger than the physical Brillouin radius ($\tilde{R}_e = 0.25$).

This section numerically proved that the scaled interior spherical Bessel gravity field can accurately capture the physical boundary of the homogeneous sphere by dropping the density to zero outside the body. This allows for accurate representation of the gravitational potential/acceleration within the scaled reference radius, expanding the convergence region beyond the physical Brillouin sphere. We have accomplished this for the simplest of all bodies: the homogeneous sphere. Next, we will look at a more general shape: a homogeneous Phobos.

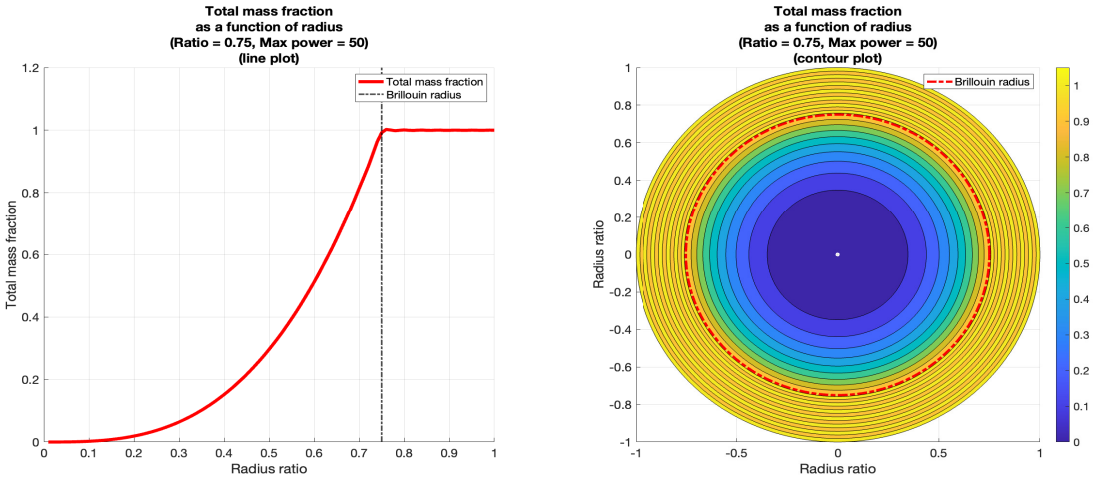


Fig. 12: Spherical mass fraction ($\tilde{m}_{sphere}(r)$) as a function of radius (left) and in contour (right) for $\tilde{R}_e = 0.75$, $l_{max} = 50$.

6.2 Scaled interior spherical Bessel harmonics for a homogeneous Phobos

As an example of a real irregular body, we use Phobos as an example. We use the same shape model with 1538 vertices employed by Takahashi and Mansell [20] (Fig. 13).

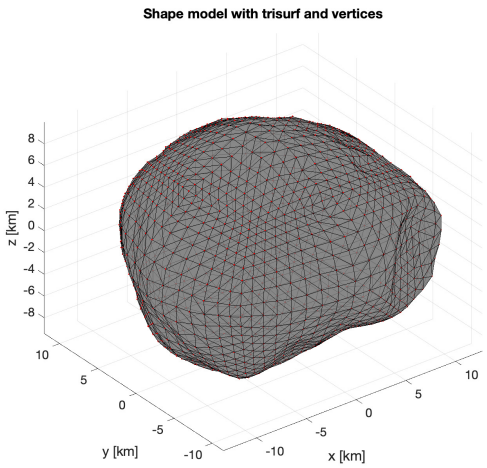


Fig. 13: Phobos shape model.

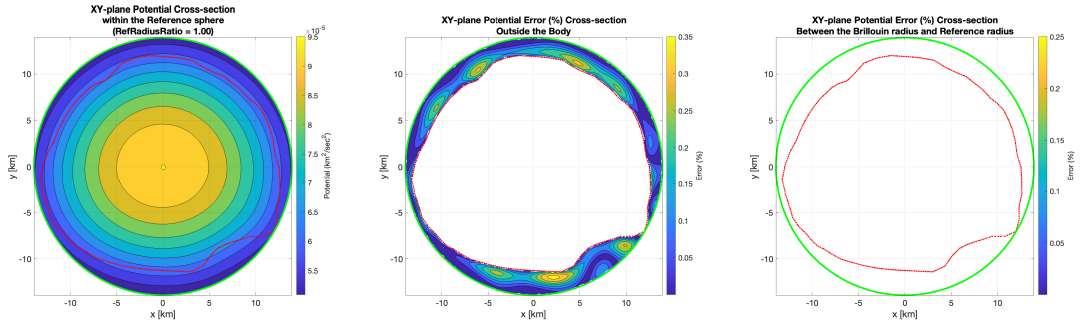
Table 1: Phobos gravity and shape model parameters.

Constant	Value
M^*	1.06511×10^{16} kg
R_e^*	13.9074 km
GM	7.108348×10^{-4} km^3/sec^2
Volume	5727.7 km^3
ρ_0	1.8596 g/cm^3

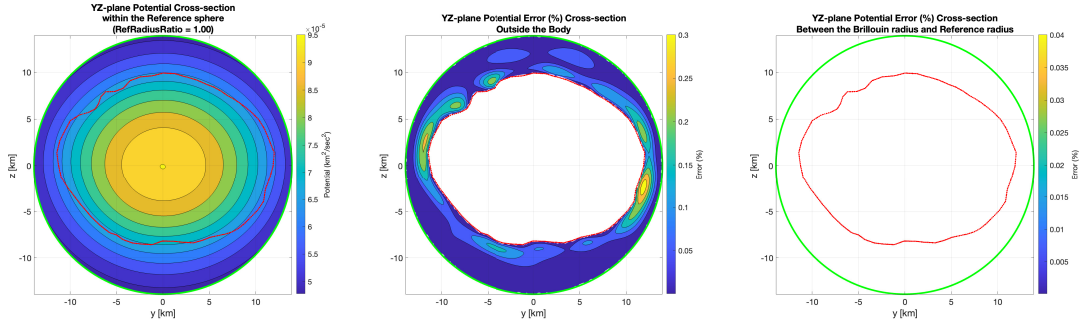
For all analysis with the Phobos shape model, we regard the homogeneous polyhedral gravity field [10] as the *truth* model. The scaled harmonics are derived from the shape model and the boundary conditions are *enforced* [20]. The parameters we employ are the same as Takahashi and Mansell [20] (Table. 1).

In order to set the benchmark for the performance of the interior spherical Bessel gravity field, we first look at the results for the unscaled reference radius ($\tilde{R}_e = 1$). Fig. 14 shows the potential comparison of a $10 \times 10 \times 5$ interior spherical Bessel gravity field with respect to the polyhedral gravity field. Because the 3D error plot renders the interpretation difficult, we only plot the cross-sections in XY (top), YZ (middle), and XZ-planes (bottom). The left column shows the potential computed from the interior spherical Bessel gravity field (i.e., the value), the middle column shows the error relative to the polyhedral gravity field outside the body, and the right column shows the same potential error between the physical Brillouin radius and the scaled reference radius. For $\tilde{R} = 1$ the physical and scaled reference radii are the same, so the plots in the right column are empty. The silhouette of the Phobos body is outlined in red dashed lines, and the physical Brillouin radius is outlined in green circles. As shown, for this $10 \times 10 \times 5$ gravity field, the potential error is less than 0.35%. Similarly, Fig. 15 shows the acceleration comparison. The total acceleration error is less than 8%.

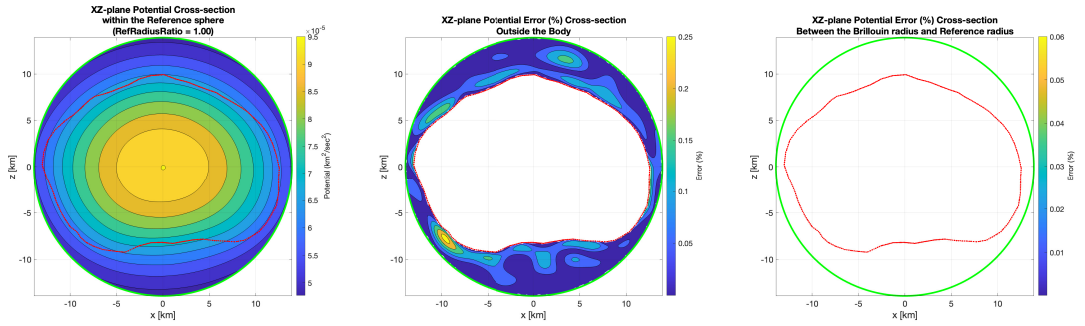
Following the potential and acceleration contour, Fig. 16 shows the density contour. The left plots show the density within the scaled reference radius, the middle plots show the density outside the body, and the right plots show the positive/negative regions of the density distribution. As expected and reported by Takahashi and Mansell [20], the density distribution does not reproduce the homogeneous density from which the harmonics were derived. This is due to the lack of one-to-one correspondence between the density distribution and the resultant harmonics. That is, a given density distribution uniquely prescribes a set of interior spherical Bessel harmonics. However, a set of interior spherical Bessel harmonics does not uniquely prescribes a density. This result may look disappointing, but the mass fractions derived earlier (Eqs. 44 and 46) exhibit remarkable properties of the interior spherical Bessel gravity field. In Fig. 17, we present that more than 95% of the mass is actually contained within the body despite the large void between the body surface and the physical Brillouin sphere. Just as the density distribution computed from the harmonics does not result in the true density distribution, the mass needs not be contained within the actual body shape. This result shows that when the field point is outside the body, the mass below the sphere adequately captures the true mass contained within that sphere. Again, this further corroborates our assertion that the interior spherical Bessel gravity field is the general form of the Shell Theorem.



(a) Potential in XY-plane.

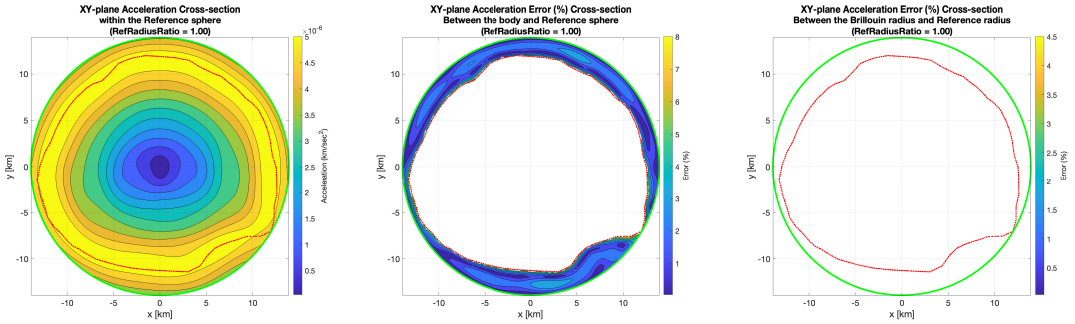


(b) Potential in YZ-plane.

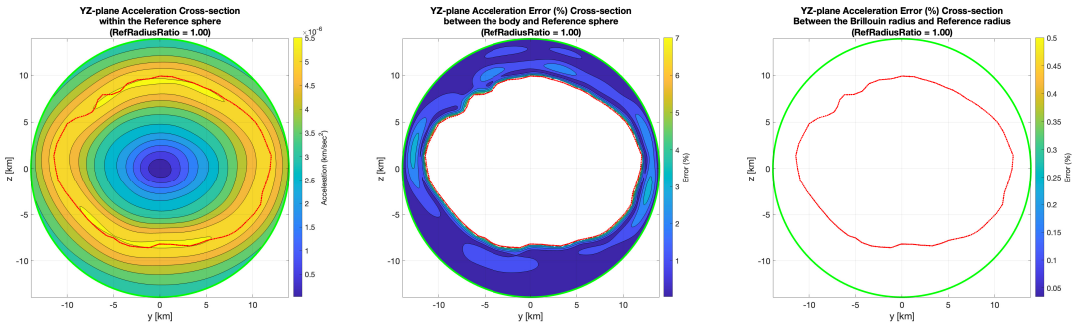


(c) Potential in XZ-plane.

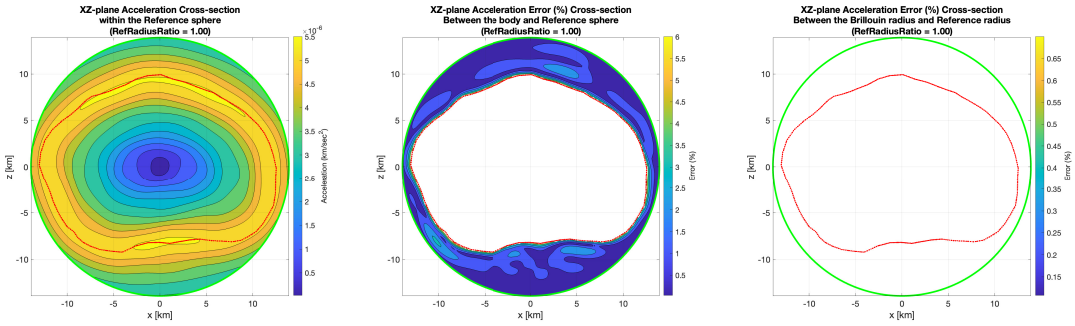
Fig. 14: Potential comparison of the scaled interior spherical Bessel gravity field with respect to the polyhedral gravity field. The degree, order, and power of the gravity field is $10 \times 10 \times 5$. $\tilde{R}_e = 1.00$.



(a) Acceleration in XY-plane.

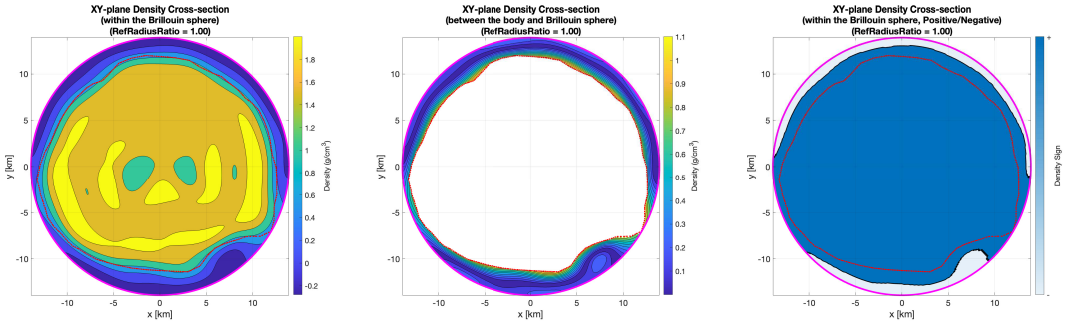


(b) Acceleration in YZ-plane.

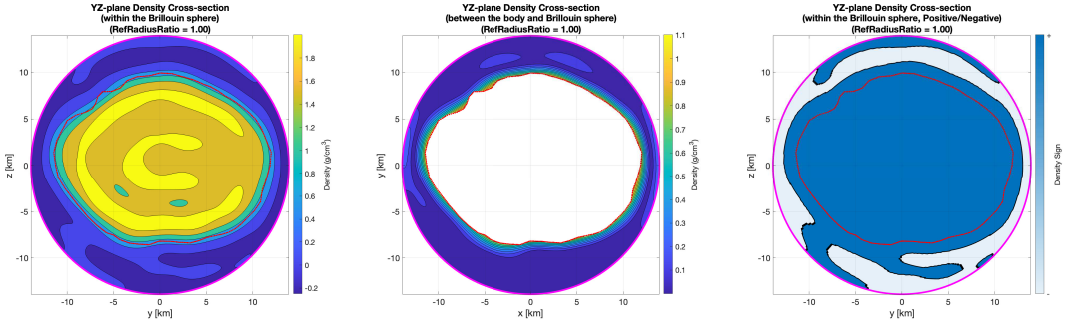


(c) Acceleration in XZ-plane.

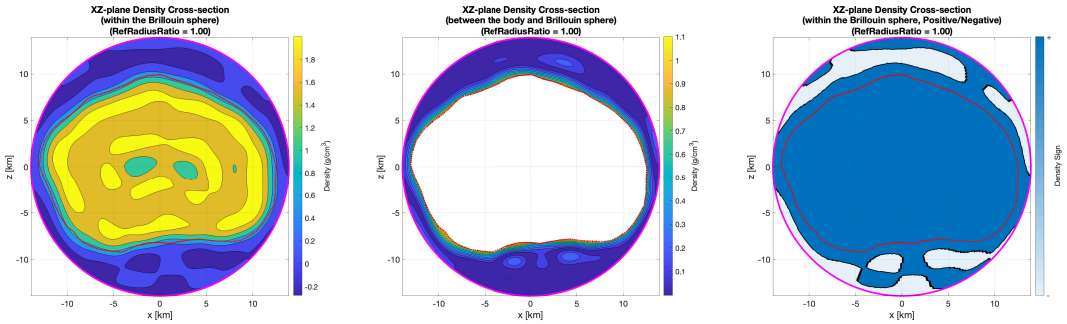
Fig. 15: Acceleration comparison of the scaled interior spherical Bessel gravity field with respect to the polyhedral gravity field. The degree, order, and power of the gravity field is $10 \times 10 \times 5$. $\tilde{R}_e = 1.00$.



(a) Density in XY-plane.

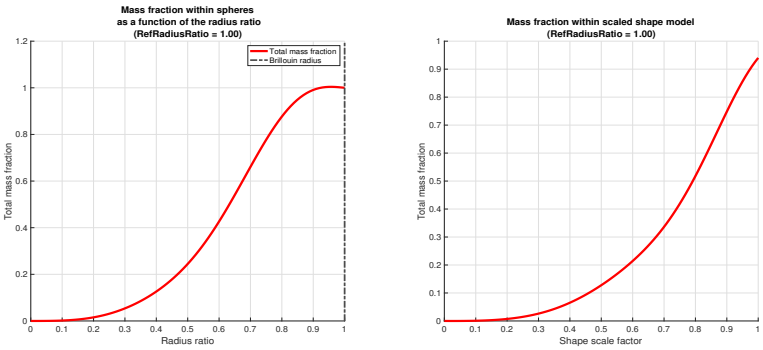


(b) Density in YZ-plane.

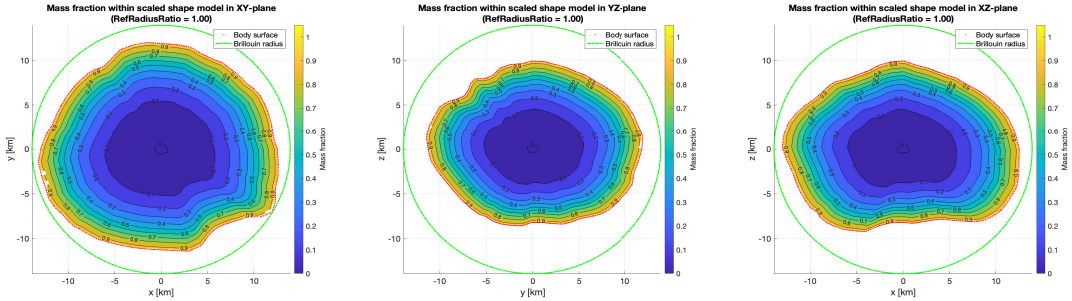


(c) Density in XZ-plane.

Fig. 16: Density distribution of the scaled interior spherical Bessel gravity field. The degree, order, and power of the gravity field is $10 \times 10 \times 5$. $\tilde{R}_e = 1.00$.



(a) Spherical and scaled shape mass fractions ($\tilde{m}_{sphere}$ in Eq. 44, $\tilde{m}_{shape}$ in Eq. 46) (line plot).



(b) Scaled shape mass fraction ($\tilde{m}_{shape}$ in Eq. 46) (contour plot).

Fig. 17: Spherial and scaled shape mass fractions of the scaled interior spherical Bessel gravity field ($\tilde{m}_{sphere}$ in Eq. 44, $\tilde{m}_{shape}$ in Eq. 46). The degree, order, and power of the gravity field is $10 \times 10 \times 5$. $\tilde{R}_e = 1.00$.

The benchmark performance of the unscaled interior spherical Bessel gravity field, particularly the mass fraction, highlighted the important properties of the interior spherical Bessel harmonics. For comparisons, we have run the same analysis for the list of gravity models in Table 2. The figures are documented in the supplemental material to save space.

Table 2

Model	Coefficients	$\tilde{R}_e$	Appendix Section
Bessel	$10 \times 10 \times 5$	0.75	Section G
Bessel	$10 \times 10 \times 5$	0.50	Section H
Bessel	$10 \times 10 \times 5$	0.25	Section I
Exterior	10×10	0.25	Section J
Bessel	$10 \times 10 \times 32$	0.75	Section K
Bessel	$32 \times 32 \times 5$	0.75	Section K
Bessel	$32 \times 32 \times 32$	0.75	Section K
Bessel	$10 \times 10 \times 32$	0.50	Section L
Bessel	$32 \times 32 \times 5$	0.50	Section L
Bessel	$32 \times 32 \times 32$	0.50	Section L
Bessel	$10 \times 10 \times 32$	0.25	Section M
Bessel	$32 \times 32 \times 5$	0.25	Section M
Bessel	$32 \times 32 \times 32$	0.25	Section M

Comparisons of figures in Section G through I show that for the same degree, order, and power gravity fields, the acceleration errors grow as the size of the scaled reference radius grows. This is expected as there is more space to model the gravity for the same number of coefficients. However, the acceleration errors within the physical Brillouin sphere remain bounded and exhibit a slow growth as opposed to, for example, an exponential growth we observe for the exterior gravity field.

While it is intuitive to think that the gravity is easier to model as the radial distance increases, it is not necessarily so for the interior spherical Bessel gravity field due to its solving Poisson's equation. The error increases faster outside the physical Brillouin radius (see Figs. G8, H15, and I22). In Fig. I22, we see close to 40% acceleration error within the scaled reference radius. Interestingly, as the reference radius increases in size, the larger errors start to appear near the edge of the scaled reference radius. Because the acceleration decays as $1/r^2$, these large percentage errors do not necessarily result in large magnitude error, however.

It is important to note that while large percentage errors are observed near the scaled reference radius, this error drops to zero due to the boundary condition with the exterior gravity field. That is, on the scaled Brillouin sphere, the potential by the *enforced* interior spherical Bessel gravity field is equal to that of the scaled exterior gravity field (see Eq. 32 and Fig. J27 for an example). These large errors in the space between the physical Brillouin radius and scaled reference radius is not a concern in real operations, because the harmonics will be estimated to yield near-zero acceleration error by the orbit determination process. At the moment we are simply performing the forward modeling based on the a priori knowledge of the density distribution. To a small extent, these errors can be blamed on the truncation error and the numerical errors due to approximating the surface integral at the center of each facet.

Increasing the degree, order, and power of the gravity field generally decreases the error near the surface of the body (e.g., Fig. H16, L36, L38, L40 for $\tilde{R}_e = 0.5$). This is precisely the opposite behavior of the exterior gravity field: the exterior gravity field diverges faster as we increase the degree and order of the harmonics outside the convergence region (i.e., within the Brillouin sphere). That is, we expect the interior spherical Bessel harmonics to become less accurate as we add more coefficients if the

convergence is not warranted. Thus, the fact that the scaled interior spherical Bessel harmonics not only manages to not diverge (i.e., remains bounded), but also becomes more accurate near the surface is a clear numerical proof that its convergence region can be arbitrarily controlled by tuning the reference radius. This is made possible by ensuring finite values for the potential on the surface of the reference sphere (Eq. 32).

On the other hand, it is also important to remember that there are two opposing effects that we observe when increasing the degree, order, and power of the interior spherical Bessel gravity field. The acceleration near the surface performs better while that between the physical and scaled Brillouin spheres degrade. Again, the degraded performance outside the Brillouin sphere is not particularly concerning for practical purposes once the coefficients are estimated through orbit determination, which we will look into shortly in the next section.

Figs. 17, G12, H19, I26 show the mass fractions for $10 \times 10 \times 5$ gravity fields with $\tilde{R}_e = 1.00, 0.75, 0.50, 0.25$. To compare, Sections N and O present the same mass fractions for $15 \times 15 \times 10$ and $32 \times 32 \times 32$ gravity fields with $\tilde{R}_e = 1.00$, 0.75, 0.50, 0.25. It is shown that, even when the scaled reference radius is four times larger than the physical Brillouin radius ($\tilde{R}_e = 0.25$), we have more than 75% of the total mass within the shape model for a $10 \times 10 \times 5$ gravity field (Fig. I26). This percentage increases to 85% for a $15 \times 15 \times 10$ gravity field (Fig. N50), and nearly 100% for a $32 \times 32 \times 32$ gravity field (Fig. O54). A careful observation of Figs. 17, G12, H19, I26, N47 through N50, and O51 through O54 reveals that the mass oscillates in larger amplitude for a smaller radius ratio (i.e., larger scaled radius) beyond the physical Brillouin sphere. That is, the mass fraction oscillates in larger amplitude to the right of the dashed lines in the left plots of Figs. N47 through N50 and O51 through O54. This is the reason for the larger acceleration errors between the physical and scaled Brillouin radii we observed earlier.

To summarize this section, we have observed that the scaling of the reference radius works effectively for a general body such as the homogeneous Phobos. There is no reason to belive that this is a special result for a Phobos shape model, and the same qualitative results shall apply to any general bodies. An accurate potential/acceleration are computed because the scaled interior spherical Bessel harmonics concentrate the mass within the actual shape of the body, corroborating our previous claim (Takahashi et al. [1]) that the interior spherical Bessel gravity field is the general form of Newton's Shell Theorem.

7 Conclusion

In this manuscript we explored the convergence region of the interior spherical Bessel gravity field and its origin. We started our journey by first revisiting the derivation of the exterior gravity field. For the exterior gravity model we have two ways to derive the desired form: separation of variables and a direct solution via the generating function (i.e., the generating solution). The former informs of the form of the solution, while the latter confers the convergence region of the gravity field. The generating solution is the origin of the Brillouin sphere that defines the convergence/divergence of the exterior gravity field.

For the interior spherical Bessel gravity field, to our knowledge, only the separation of variables exists as a viable solution. The lack of a generating solution is puzzling. We expect the same two solution methods to exist to derive the complementary gravity field to the exterior gravity field. Furthermore, we also observe that the scaling of the harmonic coefficients for a different reference radius is asymmetrically difficult for the interior spherical Bessel harmonics relative to the exterior spherical harmonics. While the exterior spherical harmonics only need a simple scale factor when the reference radius is altered, there is no such simple operation that yields the scaled interior spherical Bessel harmonics. In fact, the recomputation/re-estimation of the harmonics are necessary. We also noted that the uncertainty mapping of the gravity coefficients is invalidated when crossing the Brillouin sphere, despite achieving the global gravity field modeling with the exterior and interior spherical Bessel gravity fields.

These cryptic behaviors of the interior spherical Bessel gravity field gave rise to the hypothesis that the convergence region of the interior spherical Bessel gravity field is arbitrary, so long as the potential/acceleration of both gravity fields are continuous on the surface of the Brillouin sphere. We hypothesize that such a Brillouin sphere is any sphere that is larger than the physical Brillouin (i.e., circumscribing) sphere. That is, the boundary conditions are such that the scaled exterior spherical harmonics are weighted sum of the interior spherical Bessel harmonics with the scaled reference radius. This would allow one to expand the convergence region of the interior spherical Bessel gravity field beyond the physical Brillouin sphere, obviating the need for alternating between the exterior and interior spherical Bessel gravity fields for global gravity modeling; one can define a large enough sphere within which the field point such as spacecraft remains bounded in order to achieve global gravity modeling.

To prove our hypothesis, we revisited the interior spherical Bessel harmonics for a homogeneous sphere. We scaled up the Brillouin radius and computed the interior spherical Bessel harmonics. The result was astounding and revealed the true *potential* of the interior spherical Bessel gravity field. The resultant harmonics accurately modeled the density distribution by yielding a constant density within the body and zero outside. Such a step function is not expected in the form of the interior spherical Bessel gravity field at first glance, but its harmonics clearly contain the information about the physical boundary of the body due to the harmonics being the mass integral of the physical body. Because the density is accurately modeled, the potential and acceleration are also accurately modeled, proving our hypothesis that the convergence region can be arbitrarily made larger than the physical Brillouin sphere. This characteristic of the interior spherical Bessel harmonics further corroborates our statement in the previous publications that the interior spherical Bessel gravity is the general form of the Sir Isaac Newton's Shell Theorem.

After the homogeneous sphere, we studied the scaled interior spherical Bessel harmonics for Phobos. The potential and acceleration are well modeled within the scaled Brillouin sphere. The acceleration near the surface becomes more accurate as we add more coefficients, as expected and consistent with the previous studies by Takahashi and Mansell [20]. This result further proves our hypothesis of arbitrary convergence region for an irregular body. To understand how this is achieved, we formulated the algorithms to compute the mass contained within a certain sphere of radius r as well

as the scaled shape model as redistributed by Poisson's equation. We reveal that the majority of the mass is contained within the actual body. This behavior is consistent with the Shell Theorem, where the mass undernearth the field point precisely yields the desired potential. The drawback is that while the boundary conditions with the exterior gravity field are met, there are regions of larger potential/acceleration errors between the surface of the body and the scaled Brillouin sphere. This is due to the radial mass distribution being a function of the spherical Bessel function of the first kind, where the trigonometric functions oscillate to produce larger/smaller mass than the actual below the field point (i.e., the radial potential contains errors). The errors are more significant as the scaled reference radius becomes larger (i.e., a smaller $\tilde{R}_e$), as expected.

Our findings in this manuscript shed new light on the convergence of the spherical harmonic gravity fields. In particular, by choosing a reference radius larger than the physical Brillouin sphere, the global modeling of the gravity field is possible with the scaled interior spherical Bessel harmonics. This facillitates the gravity computation for proximity operations/grazing orbits because there is no switch necessary between the exterior gravity field and the interior spherical Bessel harmonic gravity field as the field point crosses the Brillouin sphere. In this manuscript we realize that the reference radius is merely the veil we put around the gravity field, within which we can hear the individual notes of the interior spherical Bessel harmonics. We will apply this technique to an OD problem in the future work.

Acknowledgements. The work described in this paper was carried out at the Jet Propulsion Laboratory, California Institute of Technology, under contract with the National Aeronautics and Space Administration. ©2026 California Institute of Technology. Government sponsorship acknowledged.

Data Availability. This article has no associated data.

Conflict of interest. The authors declare that there is no conflict of interest.

Author contributions. Yu Takahashi performed all the analyses in this manuscript.

References

[1] Takahashi, Y., Mansell, J.R., Matsuzawa, Y.: On the connection between Newton's shell theorem, interior spherical bessel gravity field, and special infinite series. Celestial Mechanics and Dynamical Astronomy **138**(2), 9 (2026) https://doi.org/10.1007/s10569-026-10282-6

[2] Werner, R.A.: Evaluating descent and ascent trajectories near non-spherical bodies. Technical Report NPO-46697, Jet Propulsion Laboratory (2010). url: http://www.techbriefs.com/component/content/article/8726

[3] Takahashi, Y., Scheeres, D.J., Werner, R.A.: Surface gravity fields for asteroids and comets. Journal of Guidance Control and Dynamics **36**(2), 362–374 (2013)

[4] Takahashi, Y., Scheeres, D.J.: Small body surface gravity fields via spherical harmonic expansions. Celestial Mechanics and Dynamical Astronomy **119**(2), 169–206 (2014) https://doi.org/10.1007/s10569-014-9552-9

[5] Brillouin, M.: Equations aux dériveées partielles du 2e ordre. domaines à connexion multiple. fonctions sphériques non antipodes. Annales De L'Institut H. Poincaré **4**(2), 173–206 (1933)

[6] Kholshevnikov, C.: On convergence of an asymmetrical body potential expansion in spherical harmonics. Celestial mechanics **16**(1), 45–60 (1977) https://doi.org/10.1007/BF01235729

[7] Šprlák, M., Han, S.-C.: On the use of spherical harmonic series inside the minimum brillouin sphere: Theoretical review and evaluation by grail and lola satellite data. Earth-Science Reviews **222**, 103739 (2021) https://doi.org/10.1016/j.earscirev.2021.103739

[8] Hirt, C., Kuhn, M.: Convergence and divergence in spherical harmonic series of the gravitational field generated by high-resolution planetary topography—a case study for the moon. Journal of Geophysical Research: Planets **122**(8), 1727–1746 (2017) https://doi.org/10.1002/2017JE005298 https://agupubs.onlinelibrary.wiley.com/doi/pdf/10.1002/2017JE005298

[9] Bevis, M., Ogle, C., Costin, O., Jekeli, C., Costin, R.D., Guo, J., Fowler, J., Dunne, G.V., Shum, C.K., Snow, K.: Divergence beneath the brillouin sphere and the phenomenology of prediction error in spherical harmonic series approximations of the gravitational field. Reports on Progress in Physics **87**(7), 078301 (2024) https://doi.org/10.1088/1361-6633/ad44d5

[10] Werner, R.A., Scheeres, D.J.: Exterior gravitation of a polyhedron derived and compared with harmonic and mascon gravitation representations of asteroid 4769 castalia. Celestial Mechanics and Dynamical Astronomy **65**, 314–344 (1997)

[11] MacMillan, W.D.: The Theory of the Potential. McGraw-Hill Book Company, Inc., New York (1930)

[12] Hotine, M.: Mathematical Geodesy. ESSA Monograph 2, Environmental Science Services Administration, U.S. Department of Commerce (1969)

[13] MacRobert, T.M.: Spherical Harmonics. An Elementary Treatise on Harmonic Functions with Applications. Methuen & CO. Ltd., London (1948)

[14] Heiskanen, W.A., Moritz, H.: Physical Geodesy. W.H. Freeman and Company, San Francisco (1967)

[15] Moritz, H.: Advanced Physical Geodesy. H. Wichmann, Karlsruhe, Germany (1980)

[16] Allen, A., Palmer, P.L., Papaloizou, J.: A conservative numerical technique for collisionless dynamical systems - comparison of the radial and circular orbit instabilities. Monthly Notices of the Royal Astronomical Society **242**, 576–594 (1990) https://doi.org/10.1093/mnras/242.4.576

[17] Palmer, P.L.: Stability of Collisionless Stellar Systems - Mechanisms for the Dynamical Structure of Galaxies, pp. 181–190. Kluwer Academic Publishers, Dordrecht (1994). Chap. 10

[18] Herrera-Sucarrat, E., Palmer, P.L., Roberts, R.M.: Modeling the gravitational potential of a nonspherical asteroid. Journal of Guidance Control and Dynamics **36**(3), 790–798 (2013)

[19] Takahashi, Y., Mansell, J.R.: Spherical bessel harmonic gravity expansions and their properties related to Sir Isaac Newton's shell theorem via the Riemann zeta function. AAS/AIAA Space Flight Mechanics Meeting, Hawaii (25-174) (2025)

[20] Takahashi, Y., Mansell, J.R.: Realizations of the interior spherical bessel harmonic coefficients of a polyhedral body within the brillouin sphere. Celestial Mechanics and Dynamical Astronomy **137**(2), 10 (2025) https://doi.org/10.1007/s10569-024-10231-1

[21] Arfken, G.: Mathematical Methods for Physicists, 3rd edn. Academic Press, Inc., San Diego (1985). Chap. 9, 11, 12

Supplementary Files

This is a list of supplementary files associated with this preprint. Click to download.

- supplementaldocs.pdf